

The European Space Agency's Deep-Space Antennas

These ground-based antennas, for tracking and support to interplanetary and comet observation missions, are designed to meet severe requirements for frequency stability, pointing accuracy and availability.

By ENRICO VASSALLO, Senior Member IEEE, ROLF MARTIN, ROBERTO MADDÈ, MARCO LANUCARA, PIERMARIO BESSO, PETER DROLL, GÉRARD GALTIE, AND JAVIER DE VICENTE

ABSTRACT | The European Space Agency (ESA) is today autonomously flying three interplanetary missions: Rosetta traveling to the comet Churyumov-Gerasimenko and the two orbiters Mars Express and Venus Express. The capability of supporting these and future deep-space missions is the consequence of a farsighted decision taken in 1996 to expand the ESA network of 15-m tracking antennas into the deep-space domain. The ambitious plan to provide around-the-clock coverage to all ESA interplanetary missions is almost completed: two deep-space antennas, located in New Norcia (Australia) and Cebreros (Spain), have been in operation since 2002 and 2005, respectively, while a third antenna is planned for 2011. This paper presents the two existing antennas starting from the underlying system requirements originated from the Rosetta mission, which was the most demanding in terms of required performance. The selected architecture is then described, followed by a detailed discussion about the critical performances that play a major role in deep-space support and the associated design issues.

KEYWORDS | Antennas; beam waveguides; frequency-selective surfaces; masers

I. INTRODUCTION

The development by the European Space Agency (ESA) of antennas devoted to deep-space support was triggered by the financing of several interplanetary missions. ESA's

mission model in 1996 called for a first ESA deep-space antenna (DSA1) located in Australia to track Rosetta and Mars Express; the need for a second antenna (DSA2) located in Spain, to complement these tracks and also to provide support to Venus Express and the Herschel and Planck missions to Lagrange point L2, was established in 2001. In light of the set of Martian missions belonging to the Aurora project [1], the joint ESA/JAXA BepiColombo mission, and the expected fleet on and around the Moon, the need for a third antenna (DSA3) to be located at the American longitude is being substantiated, and several host countries' sites are being investigated. The plan for DSA3, based on the availability of the necessary funding during 2008, calls for starting the development work by the end of 2008 and achieving operational status by the fourth quarter of 2011. When the third antenna is in place, ESA will be able to provide around-the-clock coverage to its interplanetary missions.

The long-term availability of frequency assignments for transmitting high-power signals and for protecting extremely sensitive receivers is one of the criteria for the antenna site selection. While the first users of ESA's deep-space antennas rely on relatively low frequency signals (2-, 7-, and 8-GHz bands), the need to support future higher rate planetary missions like BepiColombo at 32 and 34 GHz was considered from the early design phase of DSA1. Such a requirement resulted in the selection of beam-waveguide (BWG) architecture with a turning-head design along with several technological improvements in the mechanical construction.

This paper starts with the requirements and constraints that led to the selected system architecture and continues with the critical design, showing the obtained overall performances as well as the performance of the most critical subsystems. A brief discussion of further improvements being considered is included.

Manuscript received January 22, 2007; revised May 3, 2007.

E. Vassallo, R. Maddè, M. Lanucara, P. Besso, P. Droll, G. Galtie, and J. De Vicente are with the European Space Operations Centre, European Space Agency, 64293 Darmstadt, Germany (e-mail: Enrico.Vassallo@esa.int; Roberto.Madde@esa.int; Marco.Lanucara@esa.int; Pier.Mario.Besso@esa.int; Peter.Droll@esa.int; Gerard.Galtie@esa.int; Javier.DeVicente@esa.int).

R. Martin, retired, was with the European Space Operations Centre, European Space Agency, 64293 Darmstadt, Germany (e-mail: Martinrolf@t-online.de).

Digital Object Identifier: 10.1109/JPROC.2007.905189

II. SYSTEM REQUIREMENTS AND CONSTRAINTS

The key performance requirements that have driven the design and development of the ESA deep-space antennas are summarized in Table 1.

The frequency stability requirements as well as those related to the S-band and X-band gain over system temperature (G/T) and equivalent isotropically radiated power (EIRP) were driven by the need of supporting Rosetta, according to its initial mission objective consisting of an arrival to comet Wirtanen, via distances up to 6.25 astronomical units (AU) from the Earth during specific mission phases. A preliminary assessment made in the scope of the Rosetta preparation phase demonstrated that the stability performance of cesium standards, used in the ESA 15-m antennas, was not sufficient to fulfill integrated Doppler and ranging requirements for the round-trip light time values and Doppler integration times envisaged for the mission. As a result, a new frequency and time system based on active hydrogen masers had to be considered for the ESA deep-space antennas. The G/T and EIRP requirements

triggered the selection of the main reflector diameter (35 m) and cryocooled low-noise amplifiers (LNAs).

Various additional constraints had to be considered, affecting mainly the antenna system design. The need for sharing the frequency bands with terrestrial systems imposed controlling the level of the sidelobes, while the requirement of enabling simultaneous operations in different uplink and downlink bands implied the use of dichroic mirrors for separating the different bands.

III. SYSTEM ARCHITECTURE

The two deep-space antennas DSA1 and DSA2 (the second is shown in Fig. 1) have a common system architecture and employ similar or identical components at the level of mechanical, servo, radio-frequency (RF), intermediate frequency (IF), and baseband subsystems [2], [3]. The BWG systems of the two antennas are depicted in Fig. 2; the optical part starting from the shaped parabolic reflector with 35-m diameter down to the parabola M3 is conceptually identical between DSA1 and DSA2.

Table 1 Key System Requirements for the ESA Deep-Space Antennas

Performance	DSA1	DSA2	DSA3 (future)
S-Band G/T ^(*)	>39.5 dB/K	n.a.	n.a.
X-Band G/T ^(*)	>50 dB/K	>51 dB/K	>51 dB/K
Ka-Band G/T ^(*)	(***)	>55.8 dB/K	(***)
S-Band EIRP ^(**)	>98 dBW	n.a.	n.a.
X-Band EIRP ^(**)	>108 dBW	>108 dBW	>108 dBW
Ka-Band EIRP ^(**)	n.a.	(***)	(***)
Cross polarization rejection	> 25 dB		
Receive polarization	LHCP and RHCP simultaneously		
Downlink and uplink configurations	All downlinks and uplinks simultaneously		
Sidelobe envelope	1 st sidelobe: 13 dB below main beam Further sidelobes: ≤ (29-25 log ϕ) dBi for ϕ ≤ 48°, ≤ -13 dBi for ϕ ≥ 48° (DSA1) ≤ (32-25 log ϕ) dBi for ϕ ≤ 48°, ≤ -10 dBi for ϕ ≥ 48° (DSA2)		
Allan Deviation (ADEV) of the frequency reference	5·10 ⁻¹⁵ at 100 s 2·10 ⁻¹⁵ at 10000 s		
ADEV of the freq. conversion system	1·10 ⁻¹³ at 100 s 3·10 ⁻¹⁴ at 10000 s		
Group delay stability	2 ns/12 h pp		
Group delay variation in frequency over 3 MHz bandwidth	2.5 ns pp		
Phase noise density (any band)	-(51+10 log(f)) dBc/Hz for 1 Hz ≤ f ≤ 1 MHz -111 dBc/Hz for f > 1 MHz		
(*) For an antenna elevation of 10 degrees, with clear sky, including a maximum dynamic pointing error of 5.5 mdeg (3 sigma) for worst case temperature and wind conditions (50 km/h average wind speed, gusting to 70 km/h).			
(**) For an antenna elevation of 10 degrees and including dynamic pointing error.			
(*** To be defined at the time of the upgrade, based on available technology.			

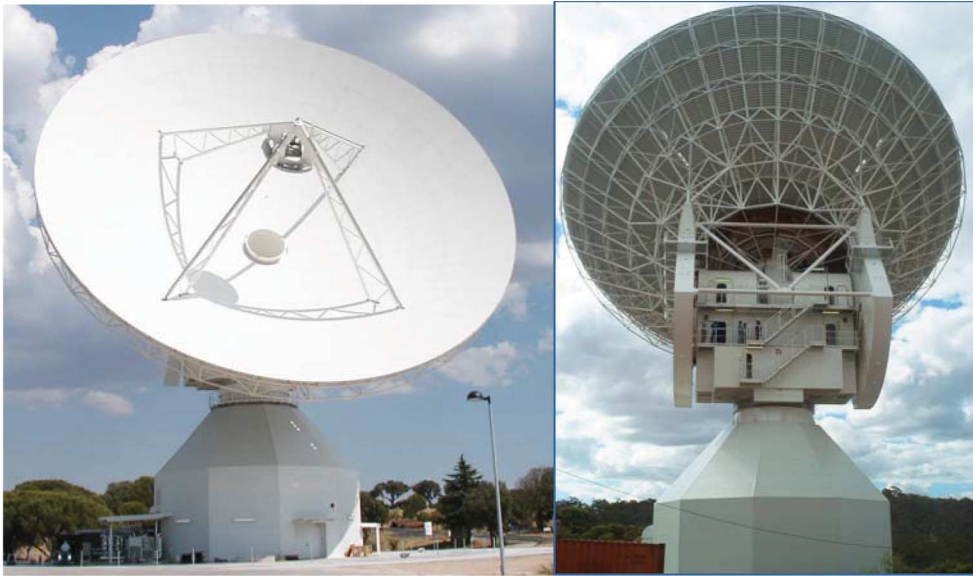


Fig. 1. ESA deep-space antenna 2 (DSA2) at Cebreros (Spain).

The mirror M4 (M4a in DSA1) is presently a flat solid mirror in both antennas and can be replaced in DSA1 by a dichroic plate passing 32-GHz signals and reflecting 2 (S-band) and 7/8 GHz (X-band) signals, in order to upgrade the downlink system to 32-GHz (Ka-band) operations. The elliptical solid reflector M5 is larger in DSA1 due to the need of supporting S-band (i.e., keeping the S-band sidelobe level under control). The subsequent flat mirrors M6 (dichroic) and M7 (solid) route the optical path to the S- and X-band feeds in DSA1 and to the X-band and Ka-band feeds in DSA2. In the future, the flat solid mirror M7 will be replaced in DSA2 by a dichroic plate passing the 34-GHz (Ka-band) uplink signal and reflecting the Ka-band downlink.

The design of the dichroic mirror M6 is critical for ensuring the fulfillment of the overall RF system performance.

The pointing accuracy is also crucial for ESA deep-space antennas, in view of the envisaged use of the Ka-band uplink and downlink bands. In the Ka-band downlink band, a pointing error of few millidegrees is sufficient for producing a measurable decrease of the received signal level and in turn a degradation of the actual antenna G/T (5.5 millidegrees pointing error yields 1.2 dB in pointing loss). The implementation of a pointing calibration system (PCS) in charge of correcting systematic pointing errors was therefore considered as a mandatory requirement for DSA2 due to the immediate need of supporting Ka-band downlink. The basic elements constituting the PCS and its interfaces to the RF and servo systems are shown in Fig. 3 [4].

The overall mechanical and servo design of the antenna system, a full motion turning head pedestal with a BWG

concept, is identical for all antenna systems. The mechanical part of the antenna system comprises an elevation structure (main- and subreflector, ballast cantilever) supported by the azimuth housing, which is mounted on top of the antenna tower. The tower also serves as the antenna equipment room, hosting the feeds and electronic equipment. The turning head design allows BWG mirrors, drive motors, and gearboxes to be located within the antenna structure to provide environmental protection and convenient access for maintenance.

The main reflector supporting structure is a truss constructed from steel pipes (Fig. 1). It also supports the quadrapod mount for the movable subreflector. The main reflector is a shaped parabolic surface. It is assembled from 304 aluminum panels. DSA1 and DSA2 use the same main and subreflector shapes. The reflector and supporting structure are counterbalanced about the elevation axis by ballast cantilevers.

The antenna system normally operates in program track mode. In this mode, time-tagged azimuth and elevation coordinates for the spacecraft orbit are supplied to the antenna control unit (ACU), which hosts the position and velocity loop of the cascade controller and interfaces directly with the servo amplifiers hosting the current loop.

Within the cascade controller [5], the innermost control loop is the current loop. The next loop is the velocity loop realized with a PI controller. The outermost control loop is the position loop, which consists of a pure P-controller. The actual positions and motions are measured by high-resolution optical encoders.

The frequency downconversion is composed of two stages: the first bringing the RF frequency from each

supported downlink band down to the L-band segment 440–640 MHz and the second at around 70 MHz, which is the input working frequency for the receivers. For Ka-band, a selectable 200-MHz-wide portion of the allocated band (500 MHz) is downconverted to L-band; this bandwidth is sufficient for future ESA missions until 2025. The selection of the frequency interval of interest is made by tuning the local oscillator of the Ka-band downconverter, in steps of 5 MHz.

Switch units allow routing each band to any demodulator, thus increasing the availability of the overall

system, which for ESA deep-space antennas is on the order of 99.5%. In particular, at least two downlink chains, each composed of an L-band downconverter and a demodulator, can be connected simultaneously to the RF downconverter used for operations.

The intermediate frequency modem system (IFMS) is the deep-space telemetry, tracking, and command (TT&C) processor in charge of all required modulation, demodulation and radiometric functions. It implements residual carrier acquisition and phase tracking, telemetry demodulation, ranging tone extraction and code correlation, and

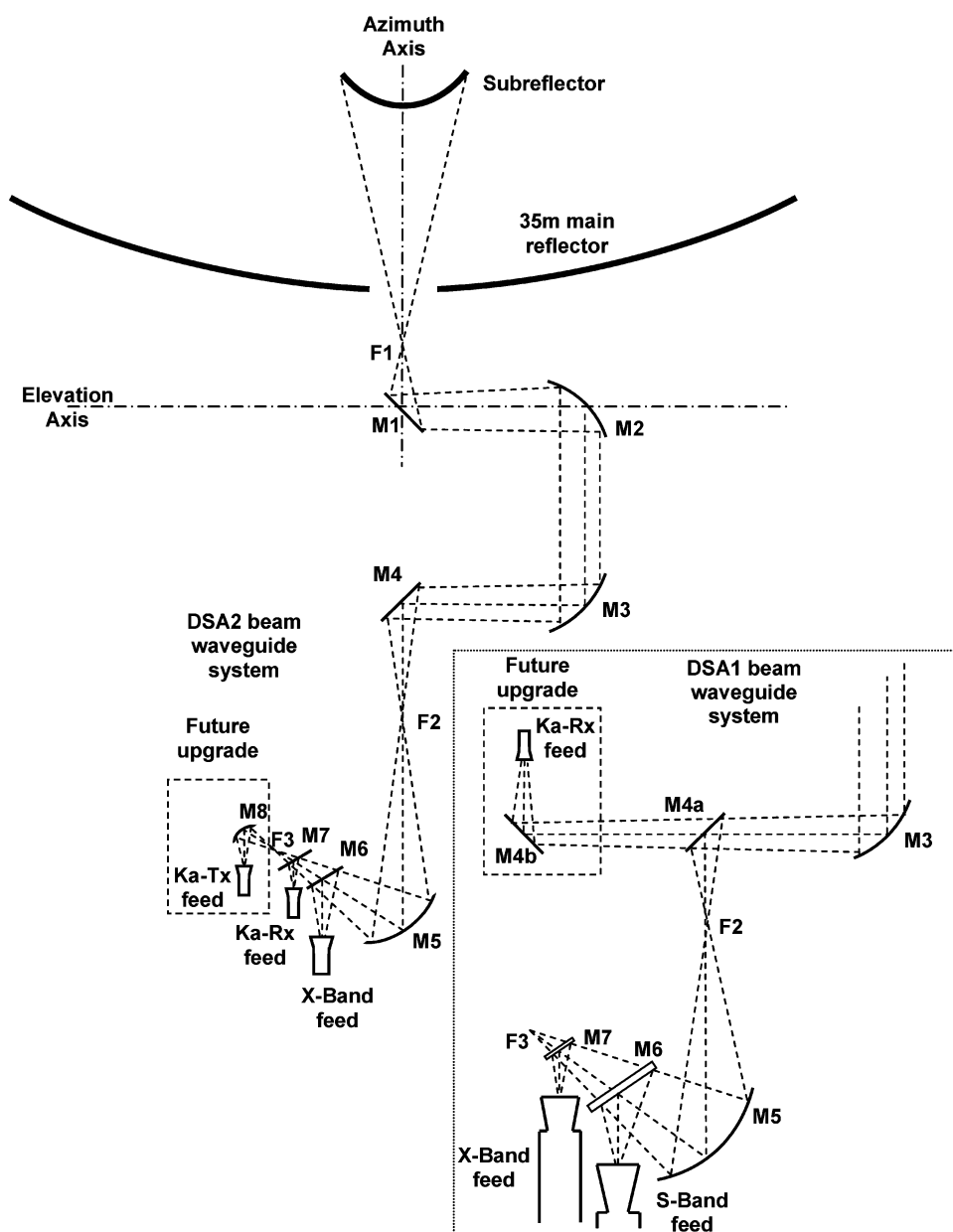


Fig. 2. Beam-waveguide system of DSA1 and DSA2.

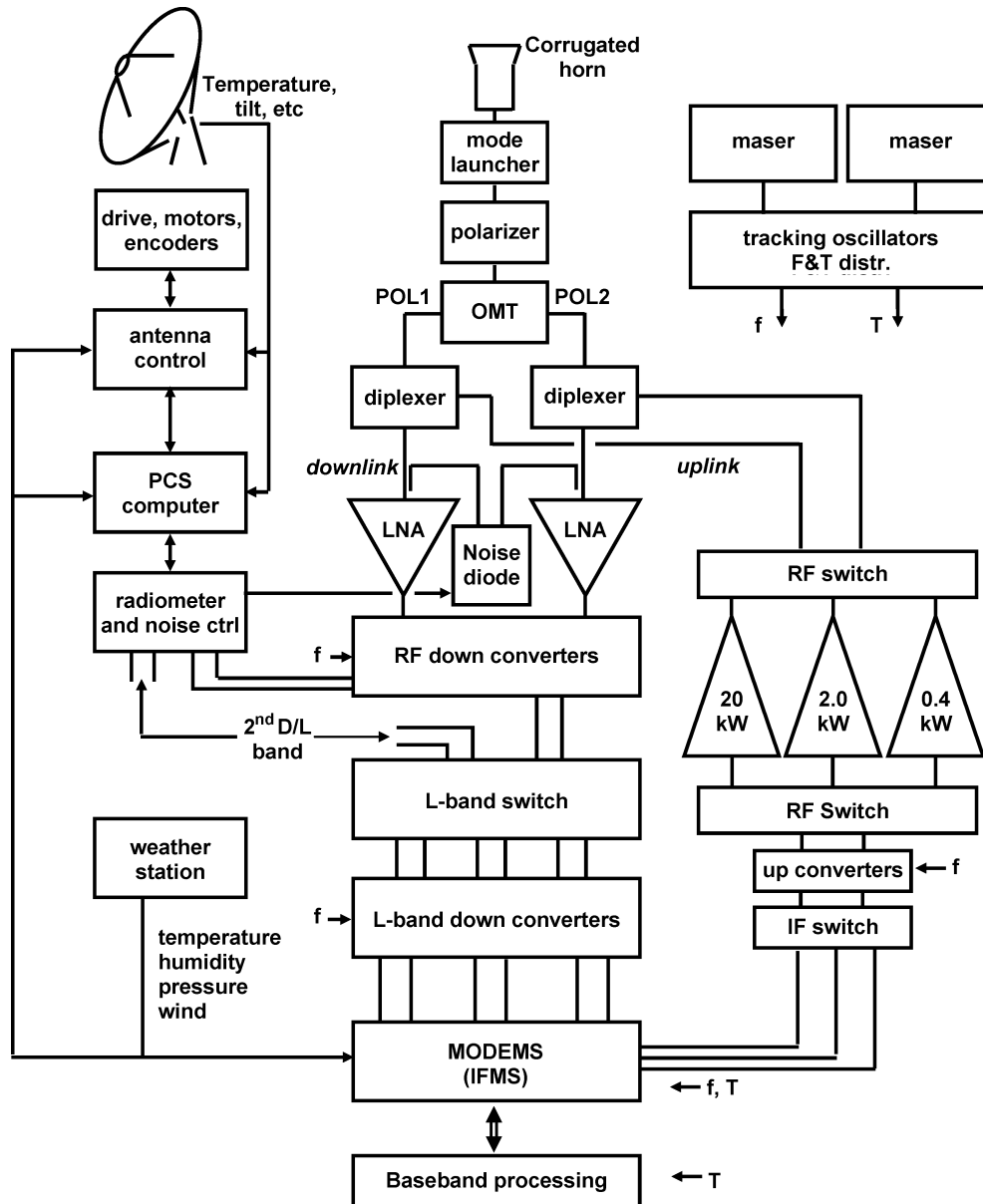


Fig. 3. System architecture of the ESA deep-space antennas. The feed (middle-top) receives the downlink signal from the BWG system. The signal is separated into the two circular polarisations in the orthomode transducer and reaches the low-noise amplifiers via the diplexers. After amplification, downconversion to 70 MHz takes place in two steps, followed by demodulation in the intermediate frequency modem system (IFMS) and baseband processing. The uplink system, on the right side, is used for upconversion of the IFMS 230-MHz output signal to the RF band and subsequent amplification and transmission to the BWG system via the diplexers. The servo system, on the left side, includes an antenna control unit, power amplifiers, motors, and encoders, used for steering the antenna according to given pointing predictions. A PCS ensures that systematic pointing errors are calibrated and removed during tracking.

recording in open loop of the complex downlink signal (I and Q components). The IFMS is also in charge of producing the IF signal at 230 MHz, modulated with telecommands and ranging video signals, which after upconversion to RF frequency and power amplification is transmitted to the spacecraft. The amplifiers of DSA1 and DSA2 can produce a maximum power of 20 kW, in S- and X-band. Operation at reduced power is possible by using

dedicated 2-kW Klystron amplifiers, or 400-W amplifiers based on solid-state transistor technology.

A maser-based frequency and time (F&T) system is in charge of distributing highly stable frequency reference signals to all frequency down/upconverters and to the TT&C processors, ensuring phase coherency of the signals along the uplink and downlink chains. The excellent stability available from the use of hydrogen maser

standards has been complemented with additional measures. A dedicated thermally controlled environment has been built for the masers, thermally stable distribution cables have been installed, and demanding phase stability requirements have been adopted for critical subsystems.

Meteorological data are important for pointing performance and for orbit determination purposes. A weather station is installed locally at the each antenna site, distributing outdoor temperature, relative humidity, barometric pressure, wind speed, and direction data to the servo subsystem.

IV. CRITICAL SYSTEM DESIGN

A. Pointing and Surface Accuracy

The requirements with respect to the pointing and surface accuracy are the key design drivers for the mechanical structure of the antennas. In a design study, which preceded the contract for the DSA1, different mechanical design concepts were studied and compared with respect to achievable mechanical performance. An advanced integrated design approach was followed such that the RF performance of the antenna took into account the effects of the structural mechanical deformations due to gravity, thermal, and wind loads.

The main and subreflector supporting structure and the azimuth housing, which are made out of steel, are not isolated or air-conditioned. To reduce nevertheless the impact of ambient temperature changes, the mechanical

structure is symmetrical to the maximum extent. A detailed finite-element (FE) model of the antenna was used to determine the mechanical deformations for different load cases including gravity, thermal, and wind effects for various elevation angles. In order to have a mechanical design with optimal performance with respect to pointing and surface accuracy, the elevation part was subject to a sequential mathematical optimization in the form of a multiobjective quadratic problem. The implemented algorithm allowed fast simultaneous optimization of different parameters of large structural FE models. The reflector truss topology, backup structure cross-sections, and azimuth house wall thicknesses were optimized for mass, surface root mean square (rms) accuracy and pointing performance under wind and gravitational loads. Furthermore, the main azimuth house wall thicknesses were designed after mathematical optimization with respect to pointing error contributions of the azimuth house. The optimization process was a basic prerequisite to achieve the specified mechanical performance. It was stopped when the predicted performance showed compliance with the specification.

As a result, the reflector supporting structure consists of a truss topology in which each truss type has an individual outer diameter and wall thickness. The supporting structure has a weight of 90 tons, which is only 25% of the total weight of the moving elevation part. The ballast cantilever (a box structure made out of steel and filled with concrete) used to counterbalance the reflector weighs 240 tons.

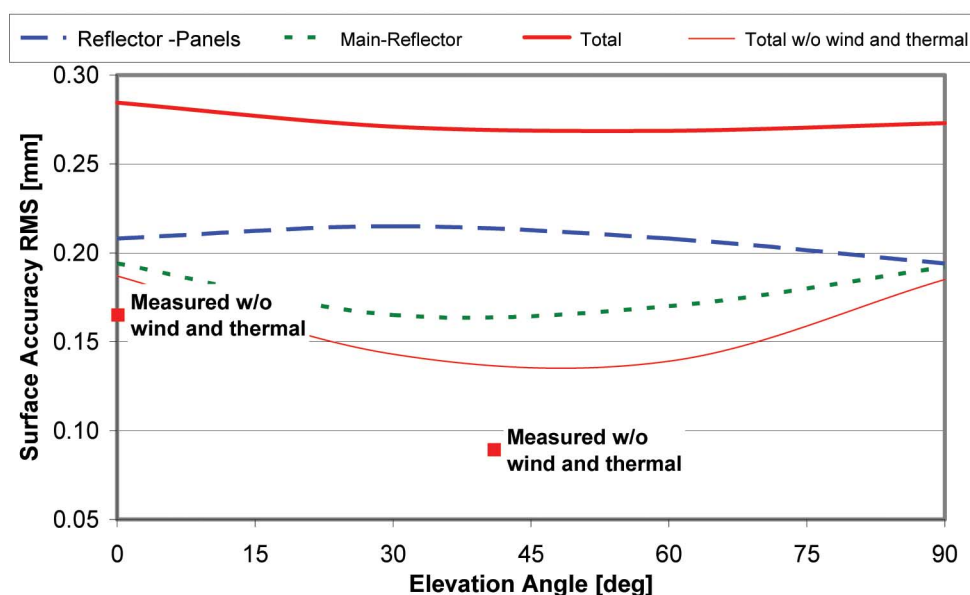


Fig. 4. Main reflector surface error versus elevation angle. The contributions of the reflector panels and of the main reflector backup structure are shown for the worst load case including gravity, wind, and thermal effects. Additionally, the measured surface accuracy for 0° and 41° elevation is shown.

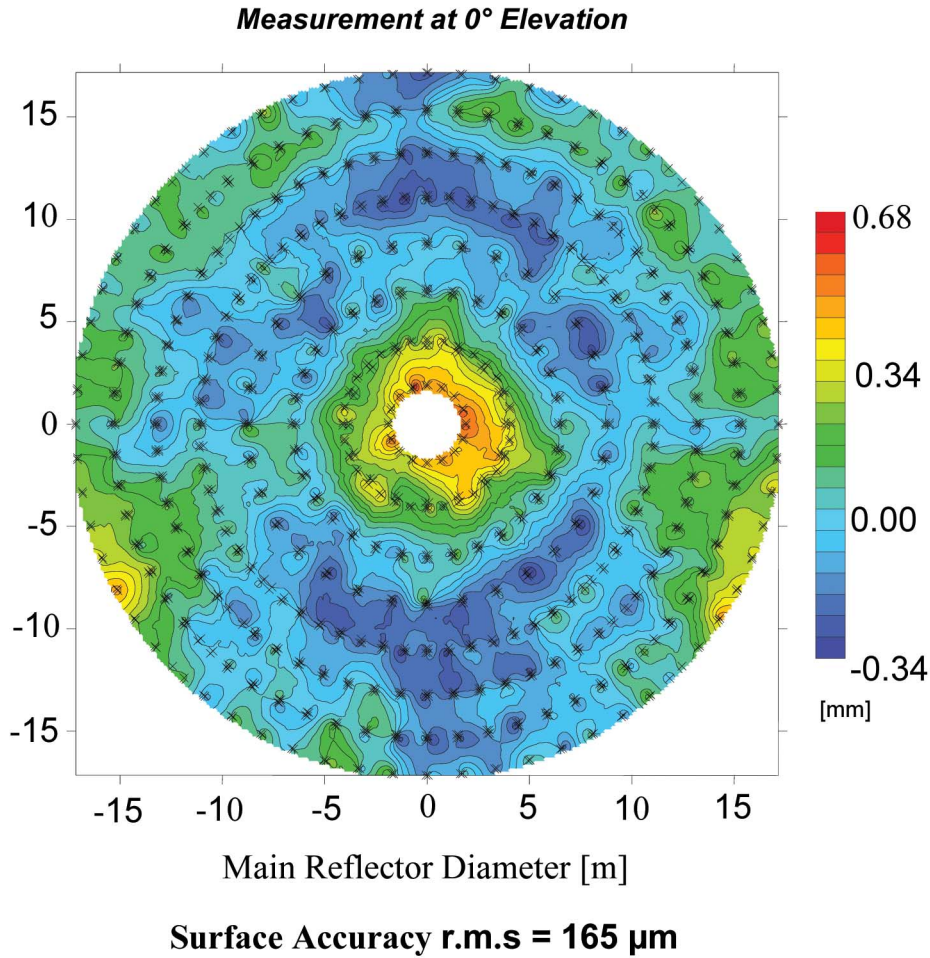


Fig. 5. Contour plot of the surface accuracy measurements performed with photogrammetry at 0° elevation. (Plot courtesy of Vertex Antennentechnik.)

In Fig. 4, the predicted surface accuracy of the main reflector is shown versus elevation. The contribution from the panels, which have a surface accuracy (always rms in the present section, or 99% probability of occurrence when explicitly mentioned) due to fabrication of 0.08 mm (measured), deteriorates due to the wind and thermal loads to approximately 0.2 mm (predicted by FE analysis). The deformation of the main reflector supporting structure contributes with less than 0.2 mm to the total surface accuracy. The predicted total surface accuracy is always better than 0.3 mm, even for worst case wind and thermal conditions, and better than 0.2 mm in benign conditions. Surface accuracy measurements performed with photogrammetry at 0° and at the rigging angle of 41° elevation confirm the predicted results. A surface accuracy error of 0.165 mm at 0° elevation was measured for nighttime conditions without wind (Fig. 5). At the rigging position, the measured surface accuracy of 0.089 mm is limited by the measurement accuracy of the photogrammetry approach. In [6], the surface accuracy of the main reflector of

the 34-m antenna DSS-24 belonging to the Deep Space Network (DSN) of the Jet Propulsion Laboratory (JPL), NASA, was measured with holography technique. At 12.5° elevation, the surface accuracy due to gravity deformations is 0.26 mm, which is nearly twice as much as the surface error of the ESA deep-space antennas.

For the subreflector, a shaped hyperboloid with 4.2-m diameter, the fabrication errors dominate the achievable surface accuracy. It is therefore constructed of cast and welded aluminum (DSA1) or welded aluminum only (DSA2). This construction method allows the very tight surface accuracy requirements to be met. A surface accuracy error of 0.065 mm at 41° elevation is achieved for nighttime conditions without wind.

To meet the specified pointing requirements, the design of the mechanical part and of the antenna servo was systematically analyzed with respect to their contribution to the overall pointing error budget. The contributions, which result in a nonsystematic error (backlash, encoder mounting, servo wind gust rejection, servo loop limit

cycle, etc.), were minimized by load-dependent backlash compensation, on-site calibration of the off-axis mounted azimuth encoder, highly optimized servo controller, and low overall friction. In particular, the servo system is a dominant source of nonsystematic pointing errors.

The simulation model used to optimize the servo controller and the servo components (azimuth bearing, gearbox, etc.) was derived from the FE model of the antenna.

The FE model consisted of approximately 18 700 elements with approximately 17 100 nodal points and around 100 000 local degrees of freedom. As models of this size are not suitable for dynamic simulations, the model sizes were reduced by modal analysis techniques. The reduced order mechanical models took into account all characteristic resonance modes in the critical frequency range up to 10 Hz.

Also the high stiffness of the elevation part contributes to the very low overall nonsystematic pointing error

contribution, which is less than 2 millidegrees (99% probability of occurrence) under worst case conditions including wind.

The systematic pointing errors introduced by gravity, misalignment, beam squint due to the BWG/feed arrangement, quasi-static thermal effects, and quasi-constant wind were minimized by design measures as far as technically and economically feasible.

To minimize the beam squint due to the BWG/feed arrangement, physical optics (PO) simulations of the full antenna optics (Fig. 6) including the BWG were based on the predicted mechanical deformations of each element as a function of gravity and azimuth and elevation position. The optimization took also into account the simultaneous reception of X- and Ka-band with left/right-hand circular polarization (LHCP/RHCP) and transmission in X-band.

Due to design measures, the sum of the raw and uncompensated systematic errors is dominated by the gravity

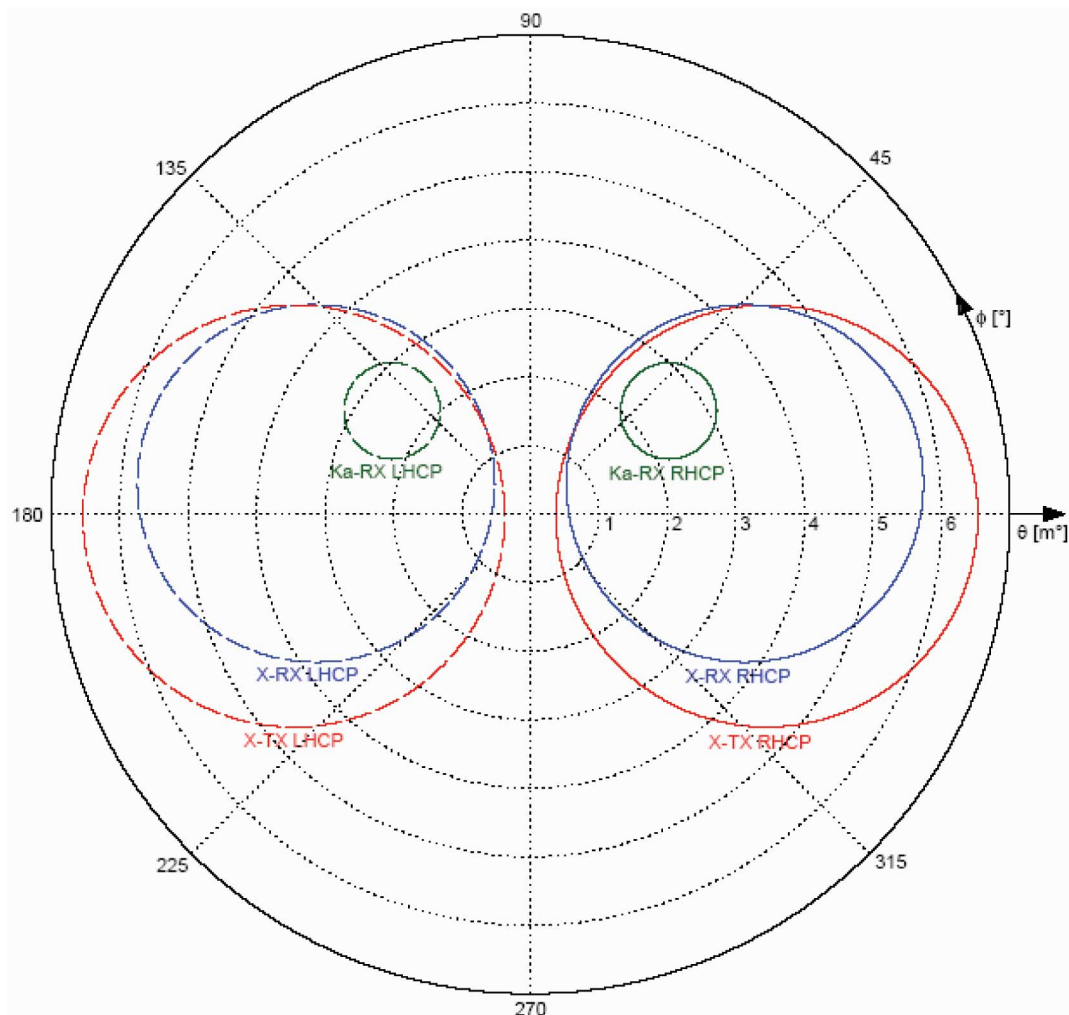


Fig. 6. RF beam squint predicted with PO simulations. (Plot courtesy of Mirad.)

Table 2 Approximate Magnitude of Uncompensated Systematic Pointing Errors

Pointing Error Source	Approximate Magnitude [mdeg]	Estimation Method
Refraction	85 at 10 deg EL 300 at 2 deg EL	Modeled, measured
Gravity	80	Measured
Misalignments, RF beam squint	15 (total)	Measured
Thermal deformations of azimuth housing	6	Measured
Thermal deformations of main reflector	2	Modeled, measured
Quasi-constant wind	2	Modeled
Wind gusts (mechanic and servo)	3	Modeled

effects and has a value of approximately 100 millidegrees (Table 2). The compensation of these pointing errors is crucial for achieving the specified pointing accuracy. The servo system has, therefore, besides a state-of-the-art servo controller, the means to compensate pointing errors introduced by gravity deformation, mechanical misalignments, beam squint due to the BWG/feed arrangement, thermal gradients, quasi-static wind effects, and atmospheric refraction. In fact, the servo system applies an

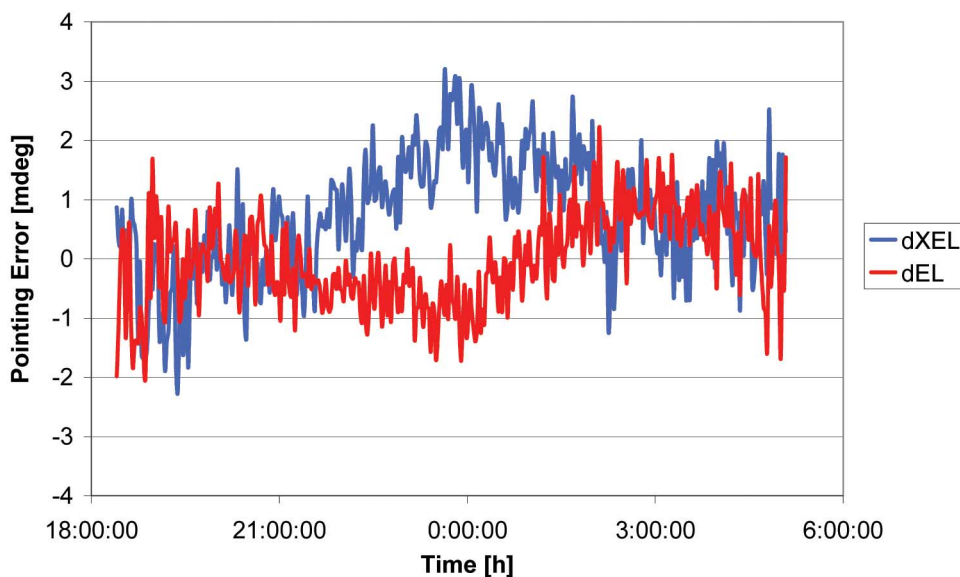
offset to the commanded azimuth and elevation positions according to the measured or derived pointing error values. Tiltmeters mounted at the elevation axis and linked to the servo system measure the quasi-static tilt of the antenna tower and the azimuth housing due to thermal effects and wind.

Thermal effects impacting the elevation part are compensated in real time: the deformation of the main and subreflector supporting structure is predicted by evaluating a thermal distortion model of the elevation part, which uses as input the readout of 252 temperature sensors mounted to the main and subreflector supporting structure.

Systematic pointing errors like gravity effects and mechanical misalignments are compensated by a systematic pointing error model (SPEM). This model consists of a set of linear-independent mathematical terms, which describe the impact on the pointing of gravity effects, misalignment, frequency band, and polarization-dependent RF beam squint as a function of the azimuth and elevation angles [7]. The coefficients, which determine the weight of each term and each effect, are determined by evaluating pointing measurements using radio stars.

For DSA1, a prototype PCS, which automates the scanning of radio star measurements, was developed and tested. For DSA2, an operational PCS was developed and integrated with the servo system [4]. This system is used to perform pointing error (PE) measurements, calculate SPEM coefficients from the PE measurements, and forward the new coefficients to the ACU.

The DSA2 PCS fully automates pointing error measurements and provides an easy tool for the calculation of

**Fig. 7.** Measured pointing error in elevation axis (dEL) and cross-elevation axis (dXEL) after applying all pointing error compensation methods when tracking a radio star for a period of 12 h.

the SPEM coefficients. This is considered as a prerequisite to having the optimum pointing performance also during day-to-day operations. Tests results for DSA2 show that the residual pointing error in both X- and Ka-band is less than 4 millidegrees (99% probability of occurrence, from 10 to 90° elevation) under benign conditions. Fig. 7 shows a set of Ka-band pointing error measurements performed in February 2006. The measurement conditions were optimal: cold and cloudless sky. Based on these measurements, which were running for 12 h, the mean radial error (MRE) is as low as 1.32 millidegrees. This figure may be compared with the MRE values published in [8] for the 34-m BWG antennas of the NASA/JPL DSN, also based on measurements: the reported values vary from 4.34 to 7.50 millidegrees.

Simulations have shown that the overall pointing accuracy degrades by approximately 2 millidegrees under worst case wind and thermal conditions. Recent observations, where the wind direction presented the worst case with respect to the elevation and azimuth position of the antenna, confirm the predictions. The servo position errors for wind speeds below 60 km/h are below 4 millidegrees (Fig. 8), leading to an overall pointing accuracy better than 6 millidegrees with a probability of occurrence of 99% under worst case environmental conditions (MRE \approx 2.5 millidegrees).

The antenna system employs an automatic subreflector positioner system, which corrects the position of the subreflector to compensate for the deflection of the main reflector and the subreflector lag over the elevation travel range. This is particularly important for Ka-band. Over the 90° elevation range, the location of the subreflector can deflect by up to 12 mm. This deflection also causes the subreflector to tilt. The effect on antenna performance is to alter the pointing direction (which the antenna servo system can compensate for) and, more importantly, to degrade the antenna efficiency.

At X-band, the gain can be reduced by up to 0.7 dB from the value at which the subreflector is aligned. For Ka-band operation, the efficiency degradation, if not compensated, would result in a gain loss of more than 5 dB. The implemented subreflector positioning system automatically repositions the subreflector to within 0.01 mm of its optimum position as the antenna elevation changes.

The calculated radiation pattern with optimal subreflector position is shown in Fig. 9.

B. Microwave Systems Design

Early in the DSA1 project, analysis indicated that to obtain the required G/T with the specified radiation

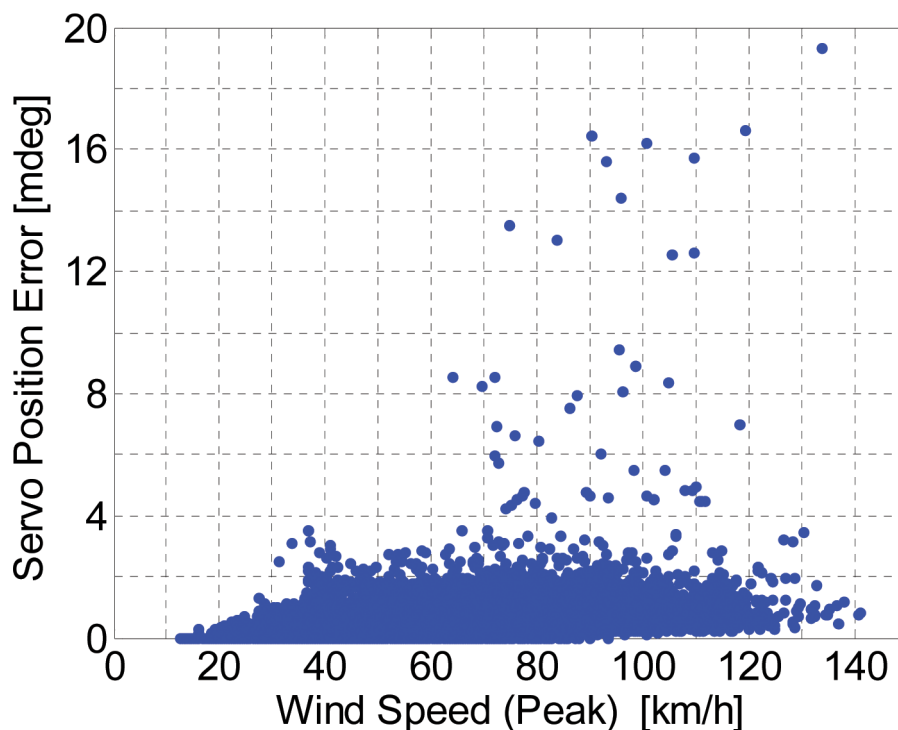


Fig. 8. Servo position error versus wind speed (peak). The wind direction with respect to the elevation and azimuth position of the antenna presented the worst case. The position errors were taken directly from the position control loop. The wind speed was measured with an ultrasonic wind sensor at a sampling rate of 10 samples/s.

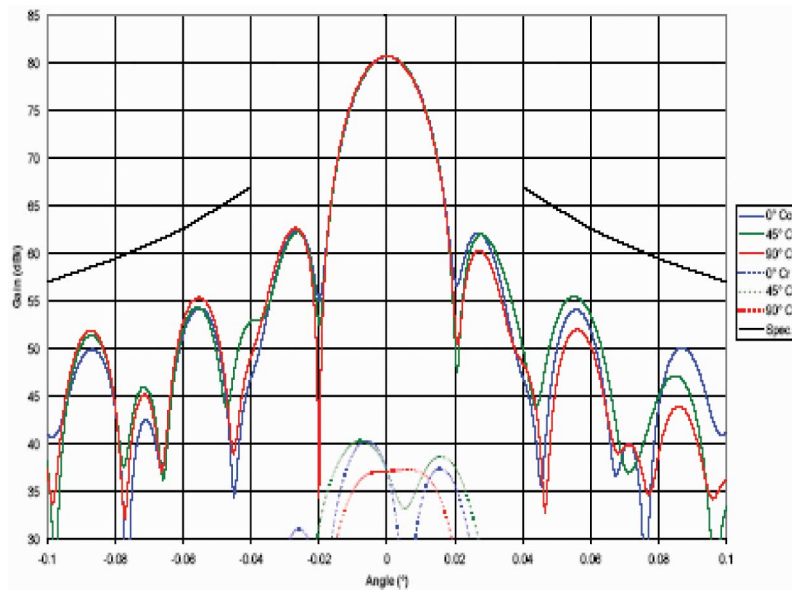


Fig. 9. Radiation pattern of DSA2, at 32 050 MHz, RHCP, with main reflector deformation at 0° elevation. (Plot courtesy of Mirad.)

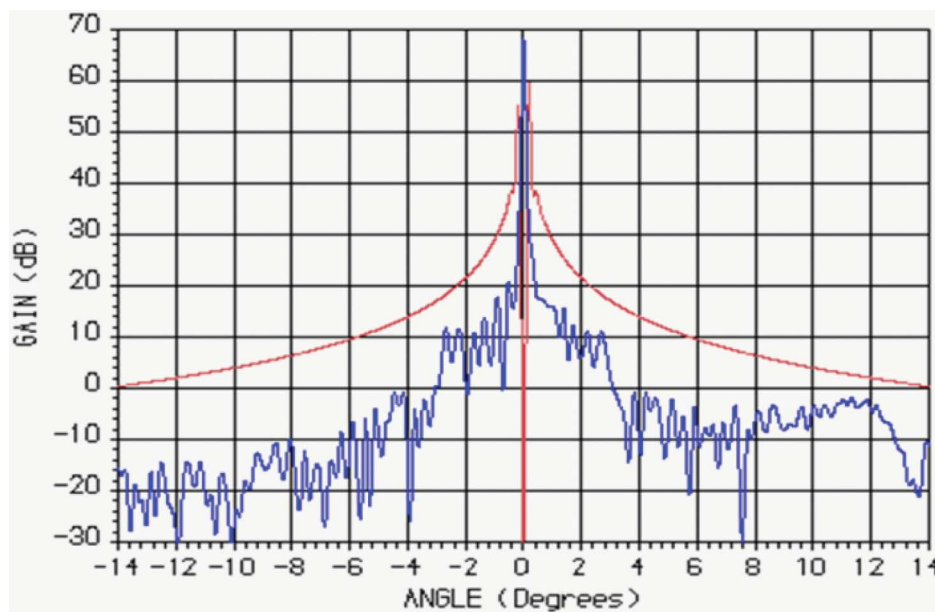


Fig. 10. DSA1 X-band radiation pattern and mask.

pattern and without maser amplifiers,¹ a shaped parabolic reflector of at least 35-m diameter was required, combined with cryogenically cooled LNAs in all bands. An “effective” F/D of 0.273 was selected to keep the third sidelobe level under control and by considering the mechanical constraints. The choice of the aperture distribution was primarily done in order to control the

¹Maser amplifiers were not considered in the design due to reliability reasons.

sidelobe level. Moreover, an aperture distribution uniform to a defined radius (6 m) and with Gaussian taper (−10 dB) to the edge of the reflector was selected. This permitted the utilization of the aperture for maximum gain and retained both sidelobe and edge spillover control. The overall RF design continued with the optimization of the BWG layout: size and position for both BWG mirrors and corrugated horns were traded off. Such an optimization was performed by Gaussian beam analysis and refined with PO analysis.

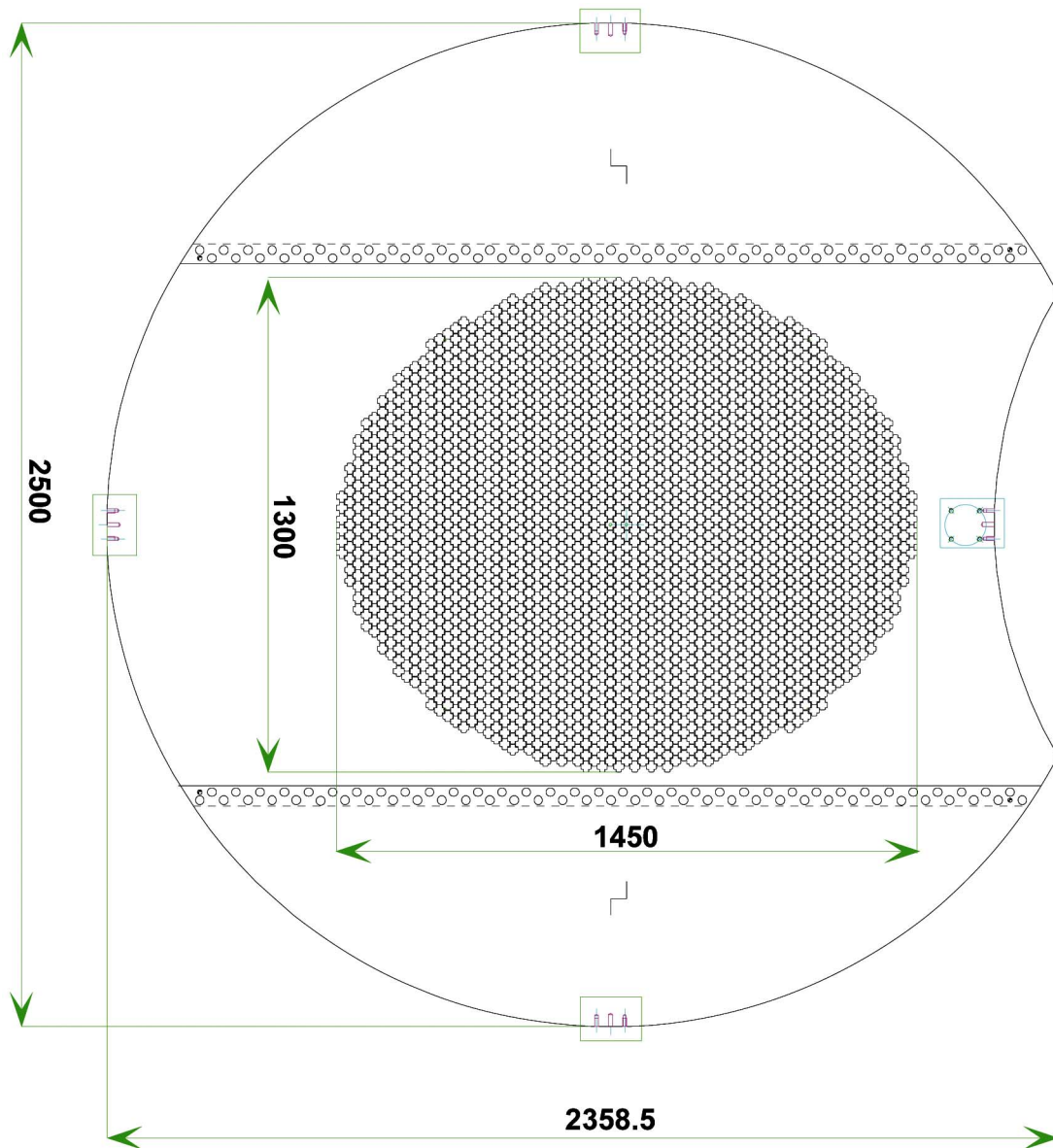


Fig. 11. Layout of DSA1 S/X dichroic mirror (M6). (Plot courtesy of Tilab.)

Special care was dedicated to sidelobe control as the BWG output created some spillover past the subreflector edge. The resulting sidelobes were dependent on azimuth rotation due to the fixed position of the M5 mirror illuminating the upper M4 mirror. The selected solution included a subreflector enlargement to 4.2-m diameter to guarantee the necessary margin to the sidelobes masks for all bands (Fig. 10).

As second step, a detailed design of the dichroic mirrors and corrugated horns, was done. The feeds are made of a corrugated horn followed by a mode launcher, a rotating polarizer, and an orthomode transducer (OMT). Particular care was devoted to the design of feed components like OMT, polarizer, and diplexer to

cope with power handling requirements (up to 25 kW in S/X-band). Mechanical and thermal analyses of these components were integrated in the RF analysis. The PO analysis of the overall architecture comprised the dichroic modeling and the effects of the mechanical deformations.

The design of dichroic mirrors was performed by following an innovative approach that not only takes into account the main incidence angle of the beam on the surface but also considers the full radiation pattern [9], [10]. Moreover, the tool used in the dichroic design was able to analyze the final machined surface by taking into account the rounding due to the manufacturing process. The DSA1 M6 mirror has a diameter of 2.4 m for S-band

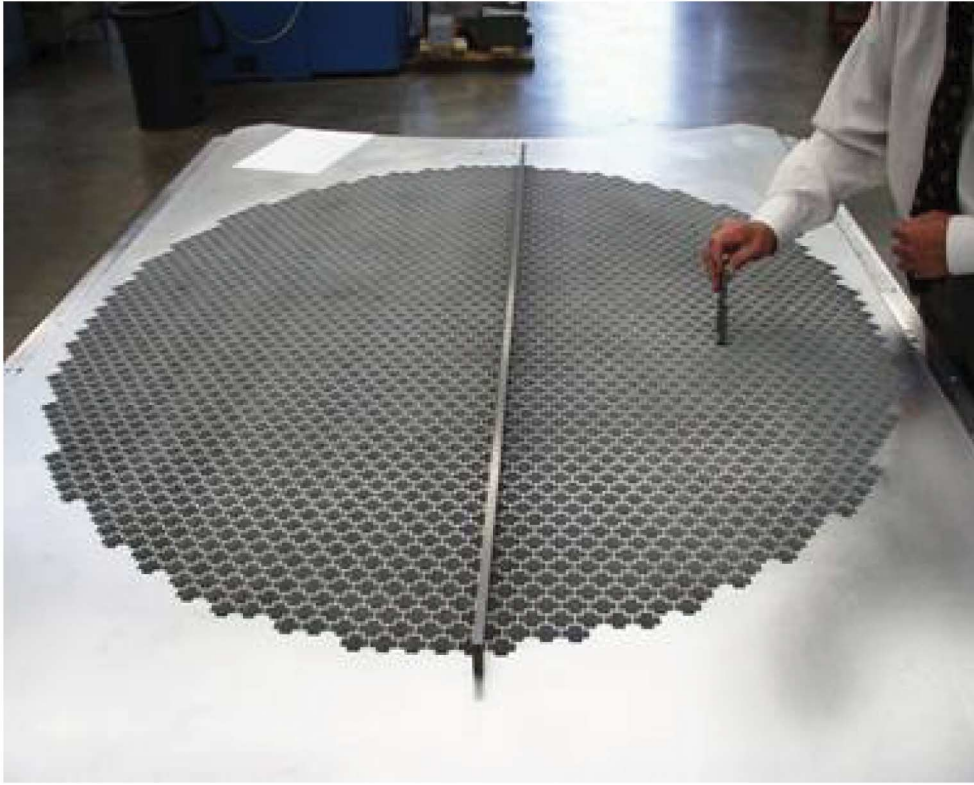


Fig. 12. DSA1 S/X dichroic. Inner segment of M6 during factory acceptance testing.

reflection with a transparent X-band dichroic area of $1.45 \times 1.3 \text{ m}^2$, as illustrated in Fig. 11.

The mirror was manufactured by a conventional milling machine and required more than 2400 cross-shaped holes, as shown in Fig. 12. Within the feed beam, the dichroic performance was measured as reported in Table 3.

The final dichroic design led to acceptance of a limited X-band cross-polarization performance (20 dB). To restore correct phasing of transverse magnetic (TM) and transverse electric (TE) modes, the X-band feed featured an additional phasing section. Factory measurement of the feed and mirror assembly demonstrated satisfactory cross-polarization rejection in X-band, better than 25 dB.

The comparison between measured and predicted X-band return loss is reported in Fig. 13, showing an excellent agreement between actual performances and results of RF simulations.

Table 3 DSA1 S/X Dichroic Performance

Performance	S-band	X-band Tx	X-band Rx
Return loss	-31 dB	<-15 dB	<-20 dB
Insertion loss	<0.05 dB	<0.19 dB	<0.12 dB
Cross polar	<-26 dB	<-24 dB	<-20 dB

The selected cross-shaped geometry is based on a similar design developed by NASA/JPL [11], [12] for their DSN. For simultaneous operations at S- and X-band, NASA/JPL installed a retractable dichroic mirror in the secondary focus of the 70-m antennas. In these installations, the dichroic can be removed if only X-band operations are required, which provides around 2 K improvement in the system noise temperature.

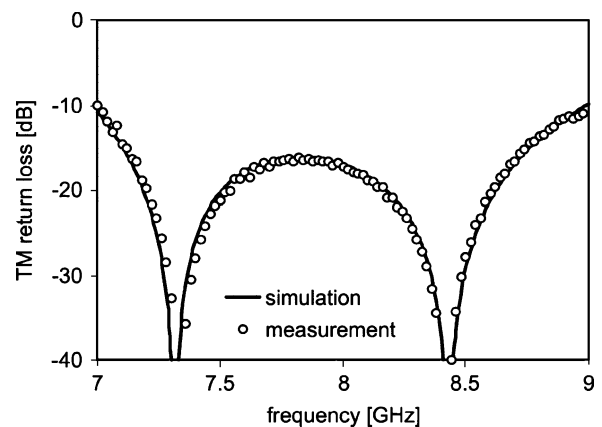


Fig. 13. DSA1 X-band dichroic return loss at 30° incidence.

Table 4 DSA2 X/Ka Dichroic Performance

Performance	X-band	Ka-band Rx
Return loss	<-30 dB	<-19 dB
Insertion loss	<0.05 dB	< 0.09 dB
Cross polar	<-30 dB	<-30 dB

For DSA2, the dichroic plate ($1.2 \times 1.2 \text{ m}^2$) was designed to reflect X-band and pass Ka-band signals. The best performance was achieved using a grid of rectangular holes. The achieved performances of the DSA2 X/Ka dichroic mirror are reported in Table 4.

NASA/JPL designed a similar dichroic mirror in the framework of the Ka-band Beacon Link Experiment (KABLE), where, together with the 32- and 34-GHz frequency bands, also the 33.6–33.8 GHz band had been used [13].

A future upgrade to allow Ka-band transmit operation in DSA2 will require an additional dichroic plate (M7). This plate will transmit the Ka-band uplink and reflect the Ka-band downlink.

The S-, X-, and Ka-band cryogenic LNA subsystems were specifically developed for use in ESA's deep-space

antennas. A photograph of the X-band LNA used in DSA2 is shown in Fig. 14. The cryogenic LNA subsystem consists of a vacuum Dewar assembly, housing a spurious rejection filter, injection coupler, and high electron mobility transistor (HEMT) amplifier, followed by a second-stage postamplifier at ambient temperature. The HEMT LNAs are cooled to 15 K by cryocoolers to obtain the noise temperature values reported in Table 5 [14].

The nominal uplink (DSA1: S and X-bands; DSA2: X-band) relies on water-cooled 20 kW Klystron amplifiers. The backup uplink function is supported by 2-kW amplifiers. For DSA2, a 400-W solid-state X-band amplifier is also included.

Concerning the RF performance of the overall system, this was found to be generally in agreement with or exceeding the requirements expressed in Table 1. As an example, various G/T measurements are reported in Fig. 15 showing a good agreement (within $\pm 0.5 \text{ dB}$) between measured values and the required performances.

C. Frequency Reference and Conversion Systems

Deep-space tracking support imposes stringent phase stability requirements on antenna equipment. In order to fulfill ESA's 0.1 mm/s navigation requirement for deep-space missions, DSA1 and DSA2 are equipped with active hydrogen masers—two in each facility for redundancy reasons. A controlled temperature environment, the distribution of the signals from the hydrogen masers to all antenna systems by means of carefully selected thermally stable cable, and phase stability requirements on critical frequency conversion and TT&C processing subsystems ensure that the navigation requirement is achieved.

The selection of hydrogen maser frequency standards mirrors the decision taken in the past by NASA/JPL, which has employed this frequency reference standard for the DSN for some years. Recently, the hydrogen masers have been supplemented with linear ion-trap/voltage controlled crystal oscillators. Cesium standards and cryogenic sapphire oscillators are also used [15], [16].

All masers used in ESA's DSA1 and DSA2 are equipped with a low-phase-noise quartz ultrastable oscillator of selected performance (single sideband phase noise $\sim -102 \text{ dBc/Hz}$ at 100 MHz, 1 Hz from the carrier). As a result, the distributed reference signal combines the best phase noise available from quartz oscillators with the excellent long-term stability of the masers. Custom-made frequency distribution units are used to provide sufficient



Fig. 14. X-band LNA including post amplifier. (Plot courtesy of Callisto.)

Table 5 LNA Performances

Parameter	S-band	X-band	Ka-band
Noise temperature	11 K	18 K	30 K
Gain	56 dB	56 dB	60 dB

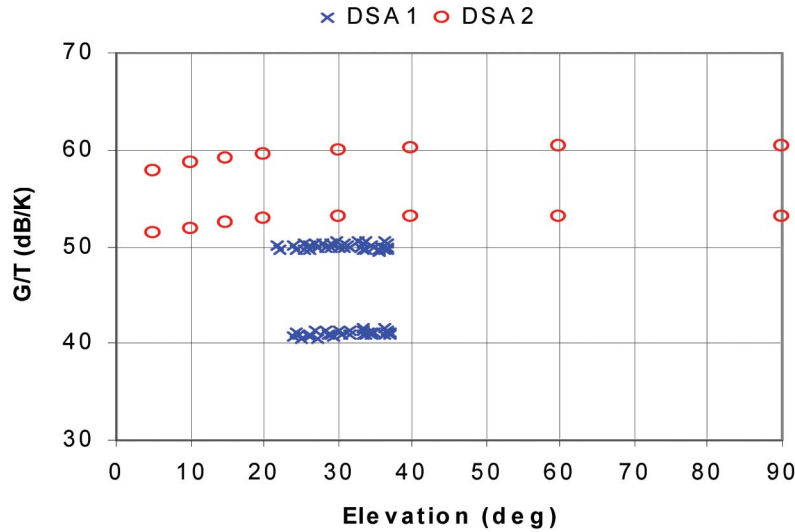


Fig. 15. *G/T measurements conducted in (blue crosses) DSA1 and (red circles) DSA2 as a function of the antenna elevation. The curves represent, from bottom to top, measurements taken in S-band and X-band at DSA1 and in X-band and Ka-band at DSA2.*

frequency outputs from the selected hydrogen maser. Based on real-time temperature measurements, these units implement a phase correction on the output signal to compensate for electrical phase variations in the complete signal chain between the hydrogen masers and the frequency outputs provided by the F&T system. Time signals, synchronized to the selected hydrogen maser are also generated. Table 6 summarizes the performance of the F&T system in DSA2 (similar performances were achieved in DSA1).

Phase-stable cables are used for the distribution of signals from the F&T system to all subsystems. In DSA2, the distribution cables can be as long as 33 m. In this case 4 ppm/°C cables are used. The environment in which these cables are installed is specified to be stable in temperature, within ± 3 °C. Actual measurements have shown that the temperature excursion generally

remains within ± 1 °C. In these conditions, the effect of the distribution cable is more than one order of magnitude better than the performance provided by the F&T system and ensures that the full performance of the masers is available at the subsystem's end.

Besides the cables used for the distribution of frequency signals, the RF cables used in the signal path (uplink and downlink) have been selected to have very low thermal sensitivity, less than 10 ppm/°C.

The frequency converters used in DSA1 and DSA2 are custom-made equipment designed to meet a demanding specification, in particular for phase noise, group delay, and phase sensitivity to temperature. Table 7 shows the phase stability performances of the frequency converters installed in DSA1 and DSA2. The achieved sensitivities ensure an excellent Allan deviation (ADEV) of the whole frequency conversion system, exceeding the requirement shown in Table 1. The ADEV of the frequency conversion system was

Table 6 F&T System's Performance

Frequency reference	100 MHz
Phase noise (dBc/Hz)	
1 Hz	-102
100 Hz	-131
Allan deviation	
1 sec	$1 \cdot 10^{-13}$
10 sec	$2 \cdot 10^{-14}$
100 sec	$3.1 \cdot 10^{-15}$
1000 sec	$8.6 \cdot 10^{-16}$
10000 sec	$5.9 \cdot 10^{-16}$
Aging	$< 2 \cdot 10^{-15}/\text{day}$

Table 7 Phase Sensitivity of ESA's Latest Generation of Frequency Converters

Frequency converter	Specification (deg/ °C)	Typical (deg/ °C)	LO Frequency (GHz)
Ka-band U/C	14	12	34.2
Ka-band D/C	12	9.3	32
X-band U/C	8	5.4	7
X-band D/C	10	3.2	8
S-band U/C	4	3.4	1.8
S-band D/C	6	1.7	1.6
L-band D/C	6	0.9	0.5

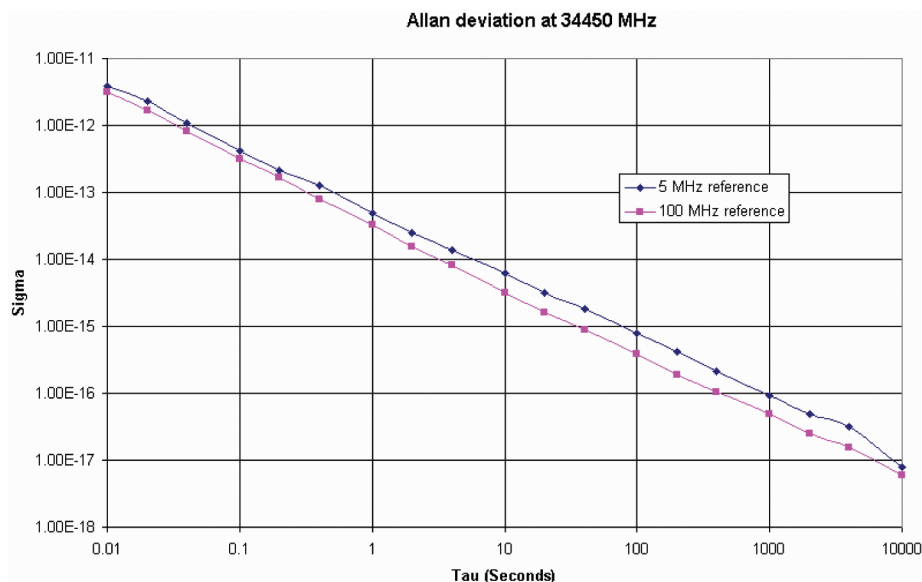


Fig. 16. Allan deviation results for the Ka-band upconverter, measured by beating two upconverters sharing the same station reference and input signal against each other.

verified by translating the uplink signal frequency to the downlink band and by measuring the unwrapped phase of the received downlink signal. The ADEV of the maser-based F&T system was verified by beating the output from two separate systems against each other.

Fig. 16 shows the Allan deviation for ESA's Ka-band upconverter. This converter will be installed in DSA2 to support future Ka-band uplink operations.

D. TT&C System

The IFMS is the TT&C processor used in all antennas belonging to ESA. The IFMS was developed in order to meet the demanding deep-space performances required by Rosetta and the other (currently flying) deep-space

missions, Mars Express and Venus Express. The performances of the IFMS make it suitable either for deep-space missions (e.g., detection of weak signals buried in noise, high Doppler and Doppler rate, phase stability and phase noise performances) or for near-Earth missions (e.g., wide input level signal dynamic).

The design of the IFMS is based on the extensive use of digital signal-processing techniques and the consequent minimization of analog hardware. A simplified block diagram of the IFMS is reported in Fig. 17.

The downlink signal is received at 70 MHz, over two polarizations. The digital downconversion block is in charge of digitizing the downlink signal by performing filtering, analog-to-digital conversion, sampling

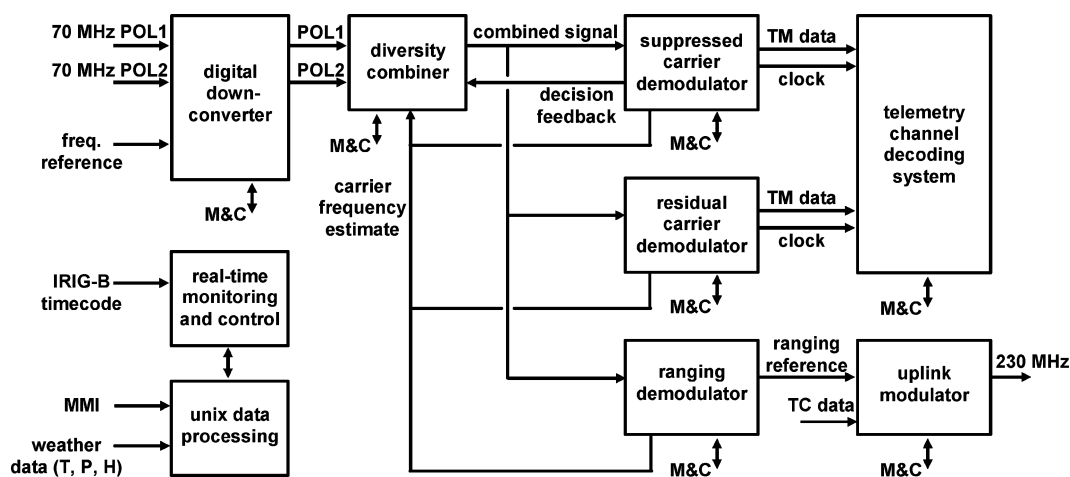


Fig. 17. Block diagram of the IFMS. (Plot courtesy of BAE systems.)

Table 8 Key Receive Performance of the IFMS

Receiver IF bandwidth	70 MHz +/-10 MHz
Signal dynamic	90 dB (nominal -15 to -105 dBm)
Carrier to noise density threshold	6 dBHz
Carrier loop noise bandwidth (2BL)	0.1 Hz to 3 kHz
Tone loop noise bandwidth (2BL)	1 mHz to 3 Hz
Ranging degradation	<1dB
Ranging threshold	$P_R/N_0 = -10$ dBHz
Phase stability	0.008 rad/K

at 280 Msps, and quantization. The resulting data stream is frequency-translated to a bandlimited decimated complex baseband signal, and in turn postprocessed for implementing the various demodulation functions. The system handles all required suppressed and residual carrier modulation schemes, with flexible configuration capabilities enabling its use in a wide range of operational conditions, ranging from deep space to near-Earth. Phase-locked loop (PLL) noise bandwidths down to 0.1 Hz (double sideband noise bandwidth) can be selected, allowing acquisition of signal when the level of the carrier-to-noise density (C/N_0) is on the order of 6 dB-Hz. Furthermore, second- and third-order loops can be selected for signal acquisition and tracking. The PLL bandwidth used for the ranging tone detection can be reduced to 1 mHz, allowing execution of ranging measurements with a minimum ranging signal over noise density of around -10 dB-Hz. Combination of the two polarizations prior to demodulation is possible for minimizing depolarization losses, with technological degradation smaller than 0.3 dB. The key performances of the receive part of the IFMS are reported in Table 8.

Moreover, the IFMS provides the decoding function, transmits the telecommands, and acts as ranging and Doppler processor. The system can also act as an open-loop receiver, providing accurately time-tagged complex samples of the downlink signal after removal of the Doppler model and filtering. Sampling rate and quantization scheme are selectable, the first ranging from a few kilohertz to around 2 MHz, the second allowing 1 to 16 bits [17]. The open-loop data produced by the IFMS are routinely used for radio science experiments, in the frame of the Venus Express mission [18], and for delta differential one-way ranging measurements [19], [20].

V. FURTHER IMPROVEMENTS

A. Correction of Beam Aberration in DSA2

Radio science operations for BepiColombo will require simultaneous downlink and uplink in Ka-band. Consequently, reception (RX) and transmission (TX) beams shall have to be pointed with a specific angular separation in

order to cope with aberration effects. A system capable of dynamically and independently steering the RX and TX beams will be required. This can be achieved by moving the Ka-band feeds and/or the position of the lower BWG mirrors M7 and M8. The prediction of the required movement for the feeds or mirrors is, however, not straightforward due to the ellipsoidal mirror M8. A so-called top-down approach was used, which considers the antenna in reception hit by a plane wave impinging with the desired beam squint angle. Such approach is based on the search for a matching between the feed/M8 radiation pattern and the radiation pattern coming from the aperture on the M5 mirror. As a result of this optimization process, the beam squint is generated by translating the M8 mirror (refer to Figs. 2 and 18) along one axis in order to squint the beam in one plane, moving both M8 and the Ka-band feed along a second axis to squint the beam in the orthogonal plane.

As the movements are fully decoupled, it is possible to combine them and squint the beam in the required directions. As a result, beam squints of 30 millidegrees can be achieved with gain degradations lower than 2 dB (Fig. 19) compared to a figure higher than 3 dB reported by NASA/JPL for their 34-m BWG antennas [21].

B. Use of the 26-GHz Band

Formerly the 25.5–27 GHz band was allocated for the use of Earth exploration category missions only. However, in 2003, this allocation was extended, allowing its use for space research (SR) services.

ESA is investigating how to best adapt the deep-space antennas, designed to support SR missions in S/X/Ka-bands, in order to cope with the 25.5–27 GHz SR allocation. The main problem is integrating the new receive frequency band within the present antenna BWG concept, feed systems, and receive chains. Different optical configurations for both DSA1 and DSA2 are under investigation. New dichroic geometries have been studied to cope with the new requirements. Fig. 20 shows the design of a frequency-selective surface able to transmit the 26-GHz band and to reflect both S- and X-band.

C. New Frequency References

The development of atomic frequency standards of improved performance provides the means for even more accurate orbit determination and opens the field to new radio science experiments. ESA currently runs two activities in the field of atomic frequency standards, with the ultimate goal of deploying improved atomic standards in its deep-space antennas. A first activity, which follows similar works performed at NASA/JPL [22], focuses on cryogenic sapphire oscillators, with the objective of improving the stability performance of the frequency reference for integration times up to 1000 s. A second activity deals with optical clocks, which are a new generation of atomic clocks expected to outperform

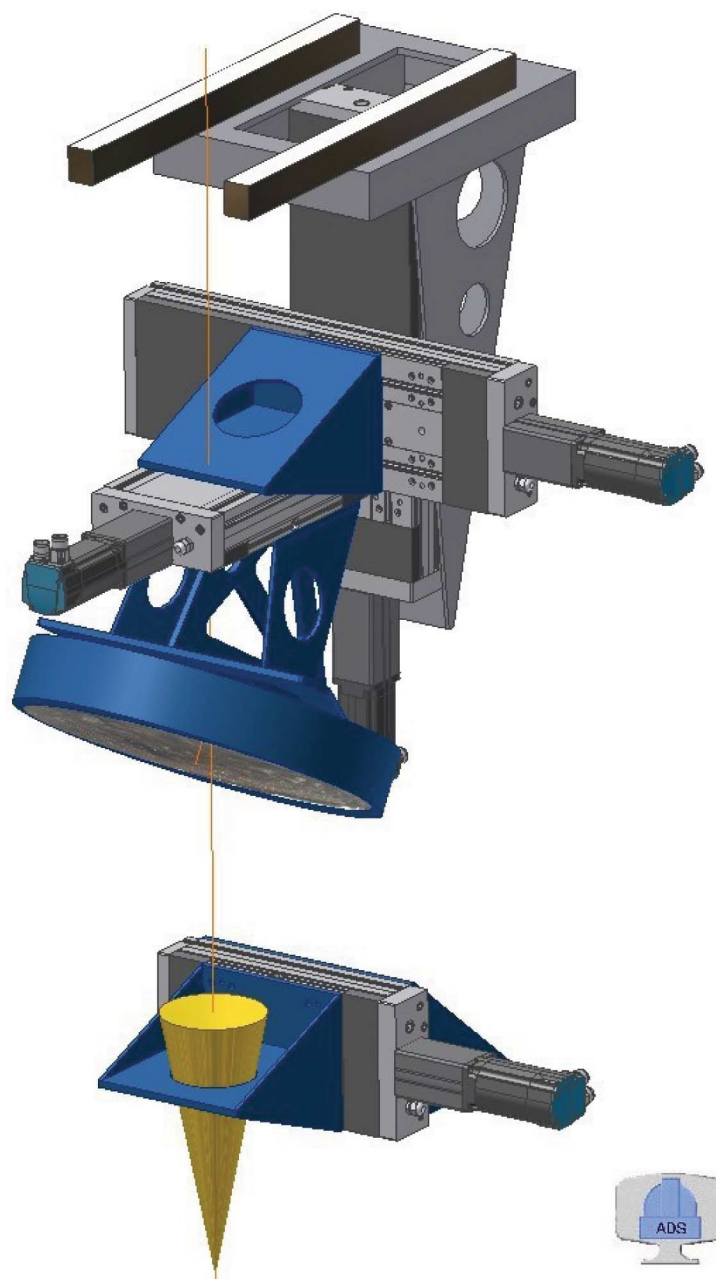


Fig. 18. Correction of beam aberration; technique based on M8 translation: geometry. (Plot courtesy of ADS International.)

current microwave standards by orders of magnitude. Due to the high stability of these clocks, ESA is investigating suitable architectures to drive the frequency converters used in its deep-space antennas, in particular at X- and Ka-band, with as few synthesis stages as possible.

D. New Generation of TT&C Processors

The IFMS hardware platform is becoming obsolete, and the processing capability is reaching its limit. It is anticipated that some future mission requirements cannot be met. Moreover, support to end-of-life of already

approved ESA missions like BepiColombo and GAIA cannot be guaranteed with the current IFMS, due to obsolescence of the current platform.

ESA plans are for the development of a new platform, covering, among others, the support to advanced modulation schemes, higher data rates (up to several hundreds of megabits per second) and larger input bandwidths up to 300 MHz (this comes from future Earth-observation and astrophysics missions). The receiver will support novel tracking techniques like wide-band ranging [23] and regenerative pseudonoise ranging [24].

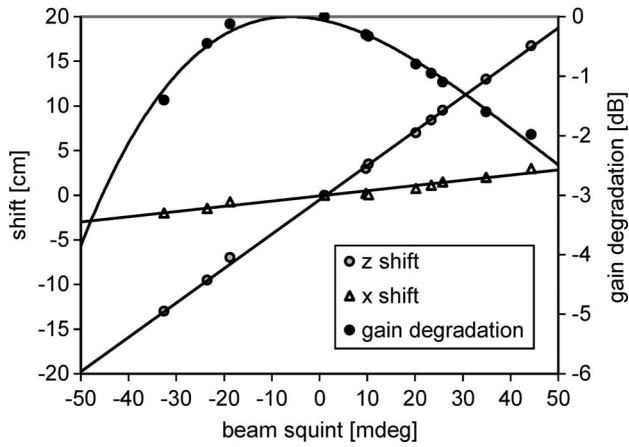


Fig. 19. Technique based on M8 translation: performance. (Plot courtesy of ADS International.)

Moreover, a higher level of operations autonomy will be considered [25].

VI. CONCLUSIONS

In this paper, we have presented the two ESA 35-m deep-space antennas, DSA1 and DSA2, located in New Norcia (Australia) and Cebreros (Spain). We have started from the definition of the key system requirements, formulated after analysis of the Rosetta mission, and then described the overall system architecture, the critical design issues in the area of the microwave, mechanical, and TT&C systems, and the achieved performance, as measured after start of operations.

Designing and implementing antennas for deep space was a challenge for ESA, as technical issues had to be faced, which were playing a minor role in the early development of the 15-m antennas. Following the analysis of internal

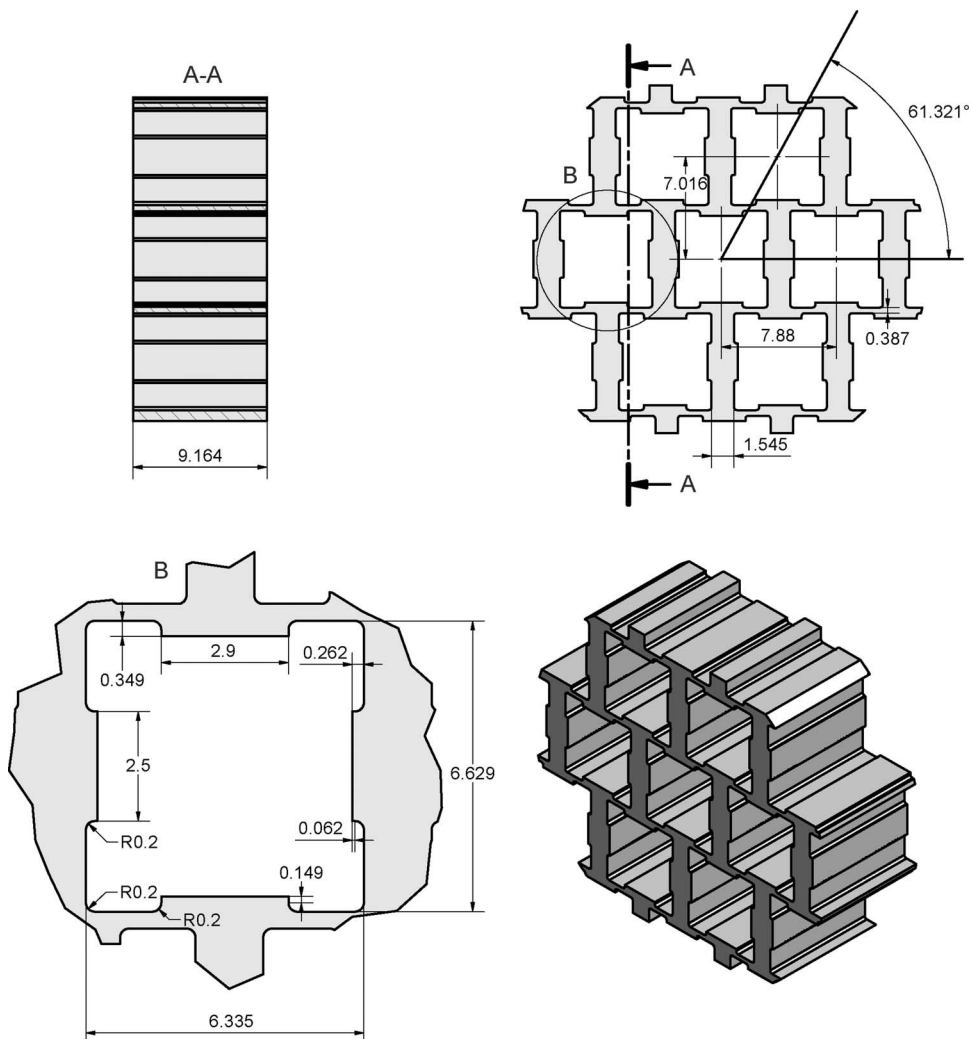


Fig. 20. Dichroic transparent in the 26-GHz band and reflective in S- and X-band (30° incidence angle). (Plot courtesy of Callisto.)

studies, and making use of the experience gained by NASA/JPL in developing their own deep-space network, ESA engineers realized that areas like pointing and microwave design, low-noise amplification, stability of the frequency reference, and deep-space demodulation were crucial for fulfilling the demanding requirements of deep-space missions.

The development of DSA1 took almost five years, whereas only three years were required for DSA2, due to the experience gained during the first project. Technology innovations were produced during the development,

mainly in the areas of the dichroic, servo, and mechanical systems. In other areas, state-of-art technology was used (20-kW high power amplifier), or developed in Europe (hydrogen masers, cryogenic low-noise amplifiers), and the related expertise was acquired.

The main difference with the DSN 34-m antennas is the selection of the turning-head concept as opposed to NASA/JPL's wheel and track design. This achieves improved mechanical performance essential for operations at higher frequencies. ■

REFERENCES

- [1] P. Messina, B. Gardini, D. Sacotte, and S. Di Pippo, "The Aurora programme," ESA Bull. 126, May 2006.
- [2] M. Warhaut and R. Martin, "Europe accesses to deep space at New Norcia (Western Australia)," ESA Bull. 114, 2003.
- [3] D. A. Akins and R. Martin, "ESA 35 m deep space antenna front end system," in *Proc. 8th Int. Conf. Space Oper. (Space Ops 2004)*, Montreal, PQ, Canada, 2004.
- [4] R. Osterried, P. Droll, and R. A. Plemel, "ESA DSA2 pointing calibration system," *Sel. Papers SpaceOps 2006*, 2006.
- [5] W. Gawronski, "Control and pointing challenges of antennas and (Radio) Telescopes," IPN Prog. Rep. 42-159, 2004.
- [6] D. J. Rochblatt et al., "DSS-24 microwave holography measurements," TDA Prog. Rep. 42-121, 1995.
- [7] P. Stumpff, "Astronomical pointing theory for radio telescopes," *Fernmeldetechnisches Zentralamt*, vol. 15. Darmstadt, Germany: Klein-Heibacher Berichte, 1972, pp. 431-437.
- [8] *DSMS Telecommunication Link Design Handbook*, "302—Antenna positioning," 810-005, Rev. E, 2004.
- [9] M. Lumpholt, K. Pontoppidan, K. van't Klooster, and P. Besso, "Analysis of frequency selective surfaces in a beam waveguide antenna," in *Proc. ESA TT&C 2001 Conf.*, Noordwijk, The Netherlands, 2001.
- [10] P. Besso, M. Bozzi, L. Perregrini, L. Drioli, and W. Nickerson, "Deep-space antenna for Rosetta mission: Design and testing of the S/X band dichroic mirror," *IEEE Trans. Antennas Propag.*, vol. 51, pp. 388-394, Mar. 2003.
- [11] W. Imbriale, *Large Antennas of the Deep Space Network*, ser. Deep Space Communications and Navigation. Pasadena, CA: Jet Propulsion Laboratory, Monograph 4, Feb. 2002.
- [12] L. W. Epp, P. H. Stanton, R. E. Jorgenson, and R. Mittra, "Experimental verification of an integral equation solution for a thin-walled dichroic plate with cross-shaped holes," *IEEE Trans. Antennas Propag.*, vol. 42, no. 6, pp. 878-882, Jun. 1994.
- [13] J. C. Chen, "X-/Ka-band dichroic plate design and grating lobe study," TDA Prog. Rep. 42-105, May 15, 1991.
- [14] S. A. Rawson and P. C. McDonald, "Development of S-, X- and Ka-band cryogenic low noise amplifiers to support ESA deep space missions," in *Proc. ESA TT&C 2001 Conf.*, Noordwijk, The Netherlands ESA-ESTEC.
- [15] *DSMS Telecommunication Link Design Handbook*, "304—Frequency and timing," 810-005, Rev. E, 2004.
- [16] J. Lauf et al., "Clocks and timing in the NASA deep space network," in *Proc. 2005 IEEE Freq. Contr. Symp. Expo.*
- [17] R. Maddè, T. Morley, M. Lanucara, R. Abelló, M. Mercolino, J. De Vicente, and G. Sessler, "A common receiver architecture for ESA radio science and delta-DOR support," *Proc. IEEE*, vol. 95, Nov. 2007.
- [18] B. Häusler et al., "Technische und wissenschaftliche Anforderungen an Radio Science Experimente zur Erforschung der Planeten VENUS und MERKUR," in *Proc. Vortrag DGLR Jahrestagung*, Stuttgart, 2002, DGLR-2002-132.
- [19] L. Iess et al., "The European Δ DOR correlator," in *Proc. Session IAC-06-CL.6.04 (IAC 2006)*, Valencia, Spain, 2006.
- [20] N. James et al., "Implementation of an ESA (DOR capability)," in *Session IAC-06-B.3.1.06 (IAC 2006)*, Valencia, Spain.
- [21] *DSMS Telecommunication Link Design Handbook*, "34-m BWG stations telecommunications interface, 104, Rev. B," 810-005, Rev. E, Aug. 1, 2005.
- [22] R. T. Wang and G. J. Dick, "Cryocooled sapphire oscillator with ultrahigh stability," *IEEE Trans. Instrum. Meas.*, vol. 48, no. 2, pp. 528-531, Apr. 1999.
- [23] P. L. Bender, N. Ashby, M. A. Vincent, and J. M. Wahr, "Conceptual design for a mercury relativity satellite," *Adv. Space Res.*, vol. 9, p. 113, 1987.
- [24] CCSDS, Pseudo-noise (PN) ranging systems, Recommended Standard, white book, Jan. 2007.
- [25] J. Hamkins and M. K. Simon, *Autonomous Software-Defined Radio Receivers for Deep Space Applications*, ser. Deep Space Communications and Navigation. Pasadena, CA: Jet Propulsion Laboratory, 2006.

ABOUT THE AUTHORS

Enrico Vassallo (Senior Member, IEEE) received the laurea degree in ingegneria elettronica from Politecnico di Milano, Milan, Italy, in 1984.

From 1985 to 1987, he was with FIAR Airborne Radar Division, Milan. His work there included analysis and development of airborne radar systems. Since 1987, he has been with the European Space Agency (ESA), Darmstadt, Germany. As a Telecommunication Engineer, he has been involved with the definition of requirements, analysis, simulation, system design, and testing of the communications equipment of ground stations and spacecraft. As Stations and Communications Manager for the Rosetta and Mars-Express missions, he has devised and specified the ESA deep-space stations as well as the modulation and coding schemes of these interplanetary missions. In 2001, he became Head of the ESOC frequency coordination office, in charge of the frequency licensing of all ESA stations and the coordination and notification of ESA satellites. He participates in the activities of ITU SG7 and corresponding CEPT groups with a view to improving space science frequency allocations. His work also includes advanced studies and international standardization activities in the field of radio frequency and modulation as well as ranging, for which he serves as Chairman of CCSDS and ECSS.



Rolf Martin was a Member of Staff of the European Space Agency and Head of the Antenna and Infrastructure Section. He spent 20 years in the German space industry (MBB, now Astrium) and has developed, managed, and implemented all antennas of the ESA Estrack network. He was the Technical Officer for the first two European deep-space antennas at New Norcia (Western Australia) and Cebreros (Spain). He retired in January 2006.



Roberto Maddè received the laurea degree in electronic engineering from Politecnico di Milano, Milan, Italy, in 1985.

He joined FIAR Spa, Space Division (now Galileo Avionica), Milan, in 1986, where he was involved in several space projects. He joined the European Space Operations Centre, European Space Agency (ESA), Darmstadt, Germany, in 1989, where he is responsible for the development of all equipment installed in ESA tracking telemetry and command systems ground stations.



Marco Lanucara received the laurea degree in electronic engineering from the University of Rome "La Sapienza," Italy, in 1994.

In 2000, he joined the Operations Department, European Space Agency (ESA), as Ground Operations Manager. Since 2003, he has been a System Engineer with the Ground Stations Engineering Division, ESA. His present tasks concern the analysis and implementation of ESA mission requirements in relation with ground-station development.



Piermario Besso was born in Chivasso, Italy, in 1963. He received the Ph.D. degree in electronic engineering from the Polytechnic of Turin, Turin, Italy, in 1988.

In 1990, he joined CSELT (now Telecom Italia), where he was involved in the design of several reflector and microstrip antennas for both on-board and ground applications. Moreover, he was responsible for the development of frequency-selective surfaces for high—and low-power application. In 2002, he joined the European Space Operations Centre, European Space Agency, as an Antenna Engineer. In 2006, he became Head of the Antenna and Infrastructure Section, Ground Station Systems Division.



Peter Droll was born in Germany in 1968. He received the M.Eng. degree and the doctoral degree in numerical methods in mechanical engineering from the Technical University of Darmstadt, Germany, in 1997 and 2002, respectively.

In 2003, he joined the European Space Operations Centre, European Space Agency, as an Antenna Mechanics and Servo Engineer in the Ground Station Engineering Division, where he is presently responsible for the antenna servo and front-end controller.



G rard Galt   received the Ph.D. degree in electronic engineering from Paul Sabatier University, Toulouse, France.

His earlier work with MATRA Space (now Astrium) focused on near-field computations and antenna measurements techniques. In 1987, he joined the Ground Station Engineering group, European Space Agency (ESA), Darmstadt, Germany. In 1996, he joined the Antenna group, European Space Operations Centre, ESA. He has been involved since 1999 on the RF system design and testing of the new ESA 35-m Deep Space Antennas.



Javier De Vicente was born in Pamplona, Spain. He received the laurea degree in telecommunications engineering from the Universidad P blica de Navarra, Spain, in 1996.

In 1998, he was a Research Trainee with the Payload Systems Division, European Space Agency (ESA), where he was involved in the simulation of microwave oscillators and the development of software tools for beamforming networks. In 1999, he joined the Ground stations division, where he originally worked on the development of tracking telemetry and command systems. Since 2001, he has been responsible for the time and frequency systems developed for ESA ground stations and their evolution.

